AGU PUBLICATIONS

JGR

Journal of Geophysical Research: Atmospheres

RESEARCH ARTICLE
10.1002/2016JD026282

Key Points:
- Robust relation found between precipitation and terrain elevation with a peak at ~1000 m asl coincident with the SALLJ moisture flux profile
- Mean precipitation depends strongly on the diurnal cycle and indicates nocturnal organization of storms into mesoscale convective systems
- Large precipitation features (MCS) are relatively rare but contribute at least 50% of the total precipitation on the eastern Andes

Supporting Information:
- Supporting Information S1

Correspondence to:
S. P. Chavez,
steven.chavez@igp.gob.pe

Citation:
Chavez, S. P., and K. Takahashi (2017), Orographic rainfall hot spots in the Andes-Amazon transition according to the TRMM precipitation radar and in situ data, *J. Geophys. Res. Atmos.*, *122*, 5870–5882, doi:10.1002/2016JD026282.

Received 22 NOV 2016
Accepted 17 MAY 2017
Accepted article online 25 MAY 2017
Published online 14 JUN 2017

Orographic rainfall hot spots in the Andes-Amazon transition according to the TRMM precipitation radar and in situ data

Steven P. Chavez[1] **and Ken Takahashi**[1]

[1]Instituto Geofísico del Perú, Lima, Peru

Abstract The Andes-Amazon transition, along the eastern Peruvian Andes, features "hot spots" with strong precipitation. Using 15 years of Tropical Rainfall Measuring Mission PR data we established a robust relation between terrain elevation and mean surface precipitation, with the latter peaking around 1000 m above sea level (asl), coinciding with the moisture flux peak of the South American Low Level Jet (SALLJ). There is strong diurnal variability, with afternoon (13–18 LT) convection in the Amazon plains, while on the eastern slopes (1000–2000 m asl), after the forcing associated with the thermal heating of the Andes subsides, convection grows during the night and surface precipitation peaks around 01–06 LT and organizes into mesoscale convective systems (MCSs). These then displace downslope to an terrain elevation of 700 m asl with stratiform regions spreading upslope and downslope and then decay during the remainder of the morning. The large MCSs contribute with at least 50% of daily rainfall (60% of the 01–06 LT rainfall). On synoptic scales, the large MCSs are more common in stronger SALLJ conditions, although subtropical cold surges are responsible for 16% of the cases.

1. Introduction

The Andes-Amazon transition, along the eastern slopes of the tropical Andes, is the rainiest region in the Amazon basin [*Figueroa and Nobre*, 1990, *Espinoza Villar et al.*, 2009]. This region is also a "hyper-hot" candidate for biodiversity conservation [*Myers et al.*, 2000]. The development of this biodiversity resulted from the interplay between rainfall, erosion, and the mountain growth [*Hoorn et al.*, 2010]. On geological timescales, orographic influence on mean precipitation is a key element for the formation of the Andes [*Horton*, 1999; *Bookhagen and Strecker*, 2008; *McQuarrie et al.*, 2008; *Barnes et al.*, 2012], although weather [*Espinoza et al.*, 2015] and climate variability are important as well [*Pepin et al.*, 2013; *Lowman and Barros*, 2014]. Models project that deforestation and climate change could result in reduced precipitation in the Amazon and reduced biodiversity, with an uncertain risk of large ecosystem changes [*Magrin et al.*, 2014]. However, the basic physical mechanisms by which the Andes control the strong precipitation in this region are not well understood and modeled, so simple approaches are often assumed. For instance, *Roe et al.* [2008] assume stable orographic ascent and adiabatic condensation, *Bookhagen and Strecker* [2008] propose small-scale relief as the main control in this region, while *Sacek* [2014] takes condensation as a function of elevation and moisture influx. Furthermore, the question of whether a relation exists at all between terrain elevation and rainfall has proven elusive in this region [e.g., *Bookhagen and Strecker*, 2008; *Espinoza Villar et al.*, 2009].

The precipitation distribution is likely the result of orographic effect on individual precipitating systems. *Liu* [2011] showed that large precipitation features (PFs; area $>$ 25,000 km^2) and systems lasting more than 12 h contribute with 50% of total rainfall in austral summer, while *Romatschke and Houze* [2013] showed that the nocturnal precipitation maximum is associated with large and medium mesoscale convective systems (MCSs) (area of radar echoes $>$ 14,700 km^2), with greater amount of wide convective and broad stratiform areas, which they proposed to be triggered by the orographic lifting of the moist South American Low Level Jet (SALLJ) [*Nogués-Paegle and Mo*, 1997; *Douglas et al.*, 1999; *Saulo et al.*, 2000; *Marengo et al.*, 2004; *Vera et al.*, 2006a, 2006b]. Above surface elevations of 1000 m above sea level (asl), the largely stable dry-to-arid environment of the Central Andes limits the development and organization of the convective systems [*Mohr et al.*, 2014]. Toward the Amazon plains, the convergence of nocturnal drainage down the eastern Andes of Ecuador and northern Peru, interacting with the warm moist air of the Amazon basin, triggers convective systems [*Bendix et al.*, 2009; *Trachte et al.*, 2010a, 2010ab; *Trachte and Bendix*, 2012].

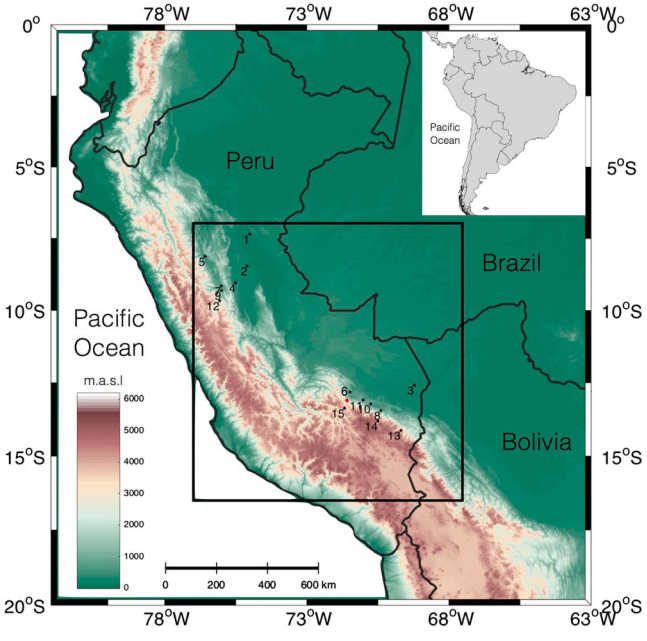

Figure 1. Digital elevation model of the region of study. The black box correspond to the region where cross sections were further analyzed. The black dots are meteorological stations used in the study. The small red line corresponds to the Kosñipata transect.

In this study we construct a very high resolution climatology and a database of precipitation features using Tropical Rainfall Measuring Mission (TRMM) precipitation radar (PR) level 2 data, similar to other studies [*Liu et al.*, 2008; *Hirose et al.*, 2008; *Romatschke and Houze*, 2010; *Liu*, 2011; *Biasutti et al.*, 2012], to characterize the spatial distribution of rainfall and orographic effects on precipitating cloud systems [*Houze*, 2012], and their diurnal cycle in the rainy season on the eastern slopes of the Andes of Peru. Also, we look for a relation between terrain elevation and rainfall using transects along the eastern slopes of the Peruvian Andes exposed to the atmospheric moisture flux from the Amazon assuming that orientation and exposure are key elements in the rainfall distribution [*Basist et al.*, 1994]. The level 2 products provide reliable observations of precipitation at global scale [*Pauluis and Dias*, 2012] and unique three-dimensional structure of rainfall and rain type classification. Level 3 gridded products rely on passive microwave measurements, which have several complications in the Andes [*Negri et al.*, 2000, *Kummerow et al.*, 2001] and do not differentiate the rain types.

2. Data

We used the 15 year (1998–2012) TRMM PR [*Seto and Iguchi*, 2007] 2A25 and 2A23 version 7 swath products [*Iguchi et al.*, 2000, 2009; *Kozu et al.*, 2009]. Version 7 has many improvements in their algorithms and is in closer agreement with the reference rainfall compared to version 6 [*Kirstetter et al.*, 2013]. The variables analyzed are rain type, height of storm (product 2A23), and estimated surface rain (product 2A25). We considered three rain types: convective, stratiform, and shallow rain. We also used a terrain digital elevation model (DEM) sampled at 3 arcsec (about 90 m) from the NASA Shuttle Radar Topography Mission; lightning data from the World Wide Lightning Location Network (WWLLN; 2005–2008), which is consistent with ground-based studies [*Virts et al.*, 2013]; and GOES infrared channel 4 (IR4, 10.2–11.2 μm) images in TIFF format from NASA (2007–2011). Daily rain gauge data were obtained from SENAMHI (Peruvian weather service). The location and time period of data availability of the stations are indicated in Table S1 in the supporting information, and only those stations at distances less than 30 km from the cross sections were selected, except stations with ids 1 and 3 in the plains and ids 12, 13, and 15 in the mountains (Figures 2c–2e). We also used annual precipitation from a rain gauge transect near the Kosñipata valley [*Rapp and Silman*, 2012]. We also used 6-hourly specific humidity and horizontal wind components from the ERA-Interim reanalysis (1998–2012 [*Berrisford et al.*, 2011; *Dee et al.*, 2011]).

3. Methodology

In this study, we constructed a $0.05° \times 0.05°$ climatology of the estimated surface rain rate from TRMM 2A25. First, we discarded pixels with rain rate of > 300 mm h^{-1}, associated with ground contamination [*Hamada and Takayabu*, 2014]. Geolocation was corrected based on surface elevation and scan angle [*Houze et al.*, 2007], and the rain rate for each swath was bilinearly interpolated to the $0.05° \times 0.05°$ grid. Finally, the gridded rain rate was averaged over the entire record, considering the total number of samples in each grid cell. This was done for the annual mean, as well as the rainy (November-December-January-February (NDJF)) and dry

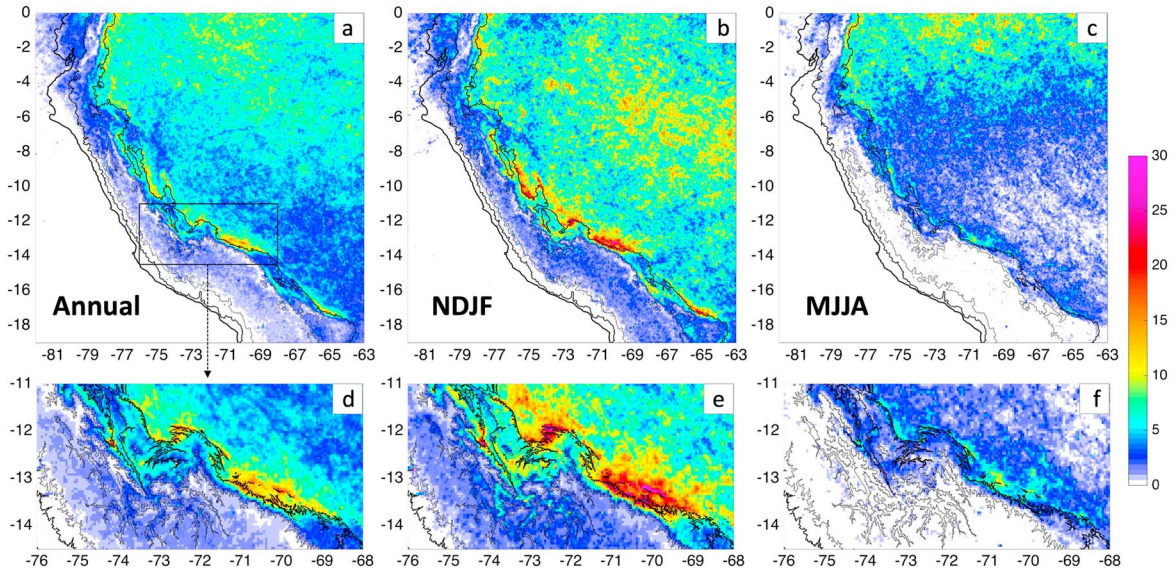

Figure 2. Mean TRMM 2A25 surface rainfall (mm/d): (a) annual, (b) wet season (November–February, NDJF), and (c) dry season (May–August, MJJA). The 1000 m and 3500 m topographic contours are shown in thick and thin black lines, respectively.

seasons (May-June-July-August (MJJA)). Approximately 140 samples were available per grid cell per month. A preliminary version of this data set used by *Espinoza et al.* [2015] reproduced the strong spatial gradients associated with the transition from the hot spots to the drier Andes, although it underestimated the precipitation relative to rain gauge data, by as much as 30% larger in the hot spots. The mean diurnal cycle was similarly estimated after first binning the data into 6 h intervals (01–06, 07–12, 13–18, and 19–20 local time or LT), resulting in similar samples sizes for each interval. We also did this for 2 h intervals to characterize the spatial evolution of the diurnal cycle. Additionally, we also calculated the NDJF 6-hourly climatology for each rain type, as well as for radar echo-top height, and the WWLLN data were used to produce a 2-hourly climatology of lightning density (number of strokes per km^2/h) for NDJF on a 0.1° × 0.1° grid. This was also done for brightness temperature calculated from the digital values from the GOES IR4 images following *Weinreb and Han* [2011], interpolated to a regular 0.05° × 0.05° grid.

We identified the precipitation "hot spots" as the areas of heavy precipitation in the eastern Andes in NDJF consisting in grid points where the mean NDJF rainfall is >12.5 mm/d within the domain 7°S–16.5°S, 77°W–67.5°W (Figure 2a). We defined "convective depth" as the difference between the radar echo-top ("storm") height and the terrain elevation, which is useful in our study zone, where the terrain elevation ranges from 200 to 5500 m asl.

From the DEM, we selected straight sections from the Peruvian Andes to the Amazon along slopes directly exposed to the Amazon basin (Figure 2a). For this purpose, the DEM was first reduced to a 2 km grid and spatially smoothed, after which we calculated the horizontal gradient. Then we selected reference points with an elevation of 1000 m asl facing the Amazon Basin, i.e., with the gradient pointing downward between north and east. The sections follow the constant direction of this vector, extending upslope for 70 km or up to the first topographic peak, whichever occurred first, and 70 km downslope, discarding those sections for which a peak exceeding 1000 m asl in the smoothed DEM was found downslope. No provision was taken to avoid sections from intersecting each other. We selected a total of 338 sections, separated by approximately by 2 km at the reference points. The topography and precipitation variables were then interpolated to each of these sections.

Using the instantaneous TRMM 2A25 swath product, we identified precipitation features (PF) as the rainy areas composed by contiguous pixels with estimated surface rain rate of > 0.15 mm h^{-1} [*Romatschke and Houze*, 2013] and grouped them according to their horizontal extension into three size categories: small (S, 25–2250 km^2), medium (M, 2250–24700 km^2), and large (L, >24700 km^2).

We calculated the horizontal moisture flux by taking the product of the 6-hourly specific humidity and the horizontal wind speed from the ERA-Interim reanalysis and then calculating the monthly climatology. We also calculated the horizontal moisture flux at 00, 06, 12, and 18 UTC (19, 1, 7, and 13 local time) by taking the product of the specific humidity and the horizontal wind speed, then we average the moisture flux in pairs 00–06, 06–12, 12–18, and 18–00 for each month in NDJF. The vertical profile of horizontal moisture was obtained as the mean of two profiles in the Peruvian Amazon at (74.75°W, 8.5°S) and (70.25°W, 12°S).

To investigate the influence of the synoptic conditions on the occurrence of precipitation features (PFs), we constructed composites of ERA-Interim reanalysis anomalies associated with all PFs and large PFs at the synoptic hours 0, 6, 12, and 18 UTC. Because some synoptic hours have several occurrences of small and medium size PFs, the number of the composites is smaller than the number of PFs; however, the number of composites for large PFs during 6–18 UTC and the number of PFs are the same (160). As explained in section 4.4, we subclassified the large PFs into southerly and northerly wind regimes in function of the meridional wind at the grid point (69°W, 12°S). The statistical significance of the wind composites was assessed with *Z* tests, so that wind vector anomalies for which at least one of the components is significant at the 95% level are considered significant.

Composites of the vertical profiles of horizontal moisture flux were produced for (i) all PFs, (ii) large PFs between 6 and 18 UTC (1–13 LT), and (iii) northerly and (iv) southerly regime large PFs between 6 and 18 UTC. We considered the mean of two grid cells in the Peruvian Amazon (73.5°W, 9°S and 69°W, 12°S). The coarser resolution of the 1.5° × 1.5° of ERA-Interim reanalysis fields used to obtain the composites does not fit the points (74.75°W, 8.5°S) and (70.25°W, 12°S) used previously.

4. Results and Discussion

4.1. Climatological Distribution

Along the eastern Andes of Peru and Bolivia, the orographic effects are primarily associated with that of the Andes on the SALLJ [*Vera et al.*, 2006a, 2006b; *Romatschke and Houze*, 2010]. In Peru, very strong year-long surface rainfall is observed in the hot spots at a terrain elevation of 1000 m asl, extending slightly to the east (Figure 2a). The precipitation in the Peruvian Amazon and, particularly in the hot spots, is much larger in NDJF (Figure 2b) than in MJJA (Figure 2c), as the former is the monsoon season in South America, with strengthened moist air transport by the low-level trade winds from the tropical Atlantic Ocean to the Amazon Basin, and southward along the Andes through the SALLJ [*Berbery and Barros*, 2002; *Marengo et al.*, 2004, *Vera et al.*, 2006a, 2006b], resulting in higher humidity in the Peruvian Amazon [*Kishore et al.*, 2011] and greater moisture convergence on the eastern Andes [*Espinoza et al.*, 2015]. However, even in MJJA, the precipitation in the hot spots is much greater than in the surroundings (Figure 2c), indicating that the orographic effects on the weaker SALLJ are still active. In contrast to previous analysis based on in situ data [*Figueroa and Nobre*, 1990; *Espinoza Villar et al.*, 2009] or even on TRMM [*Bookhagen and Strecker*, 2008], in our analysis we observe finer spatial structure. For instance, the largest of the precipitation hot spots (13°S–14°S) is formed by two narrow parallel bands separated around 30 km in both the annual mean and NDJF (Figures 2a and 2b). One is centered at the 1000 m asl level on the main eastern slope, while the other (stronger) one appears to be in the plains, but on closer inspection (Figures 2d–2f), the high-resolution DEM indicates that it is located slightly upstream (to the northeast) of the top of a low mountain chain located between the Puno and Madre de Dios regions, with peak terrain elevations of around 1000 m asl (Figures 2d–2f).

The Andes act as an effective barrier to the moisture flux from the Amazon, resulting in an abrupt decrease in precipitation at terrain elevations above 3500 m asl (Figures 1 and 2a), consistent with rain gauge data [*Espinoza et al.*, 2015] and previous TRMM-based studies [*Bookhagen and Strecker*, 2008; *Nesbitt and Anders*, 2009; *Biasutti et al.*, 2012; *Rasmussen et al.*, 2016]. However, rainfall is substantial along major inter-Andean valleys that intrude from the Amazon into the Andes in NDJF (but not MJJA). This suggests that the valleys channel the moisture flux from the Amazon, feeding the precipitation in the valleys and their surroundings, a key element for water resources in the Peruvian Andes, particularly clear for the Pampas, Pachachaca, and Apurimac valley system (13°S–15°S, 74°W–72°W; Figure 2 [*Perry et al.*, 2013]).

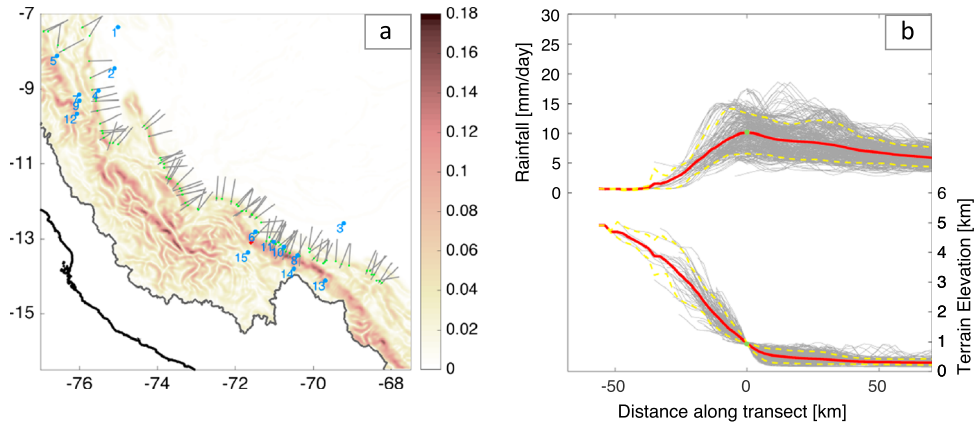

Figure 3. (a) Map of the study region and the topographic slope (shading) for the Amazon basin, indicating a subset of the 338 cross sections (gray lines with 1 km elevation as a green dot) selected to analyze the relation between TRMM 2A25 rainfall and orography. The blue dots are meteorological stations (see main text). (b) Rainfall (top) and terrain elevation (bottom) profiles (gray lines) along the cross sections in Figure 3a. Also shown are the mean (red solid line) and the 10 and 90 percentiles (yellow dashed lines).

4.2. Relation Between Rainfall and Terrain Elevation

Along the sections down the eastern slopes into the Amazon, the annual mean precipitation maximizes around the reference points (1000 m asl) and decreases slowly toward the Amazon basin, but decreases sharply in the upslope direction, becoming substantially smaller at elevations around 3500 m (Figure 3b). These results are not sensitive to changing the elevation of the reference points to 1300 or 700 m asl. By binning rainfall with respect to the elevation along these sections, we found a robust relation between terrain elevation and rainfall (Figure 4c) that shows maximum precipitation at a terrain elevation of 1000 m asl in the annual, NDJF, and MJJA means (Figures 4a–4c). The precipitation in the inter-Andean valleys also approximately follows this distribution (not shown). The geographical variability of the mean precipitation along the eastern Andes, indicated by the range between the 10 and 90 percentiles between the transects, which is particularly large (>20 mm) at an elevation range of 1500–2000 m asl in NDJF (Figure 4b), was associated with the precipitation of the largest hot spots extending further upslope (e.g., Figure 2e). The vertical distribution and its seasonality follow closely the profile of the horizontal moisture flux associated with the SALLJ, which maximizes around 1000–1200 m asl, slightly higher than the precipitation peak (Figures 4a–4c). This suggests that the rainfall-elevation relation is not determined by local upslope processes as much as by the vertical profile of the horizontal moisture convergence, consistent with *Romatschke and Houze* [2010]. We note that the horizontal wind was associated with the SALLJ peaks around 1500 m asl [*Marengo et al.*, 2004], but since specific humidity decreases strongly with altitude, the moisture flux is more bottom-heavy. In situ measurements of the SALLJ moisture flux profile, however, are lacking in this region.

The rainfall-elevation relation from TRMM is similar to the one suggested by the rain gauge observations available near the sections (Figures 4a–4c), although the values for the rainiest stations (Quincemil and San Gabán, ids 10 and 8, respectively) is around 40%, 35%, and 60% greater than TRMM PR for the annual, NDJF, and MJJA means, respectively, consistent with *Espinoza et al.* [2015] and with other studies that indicate that the TRMM PR underestimates precipitation rates associated with deep convection over land [*Iguchi et al.*, 2009; *Kozu et al.*, 2009], particularly in South America, where it exhibits a negative bias of ~40, 25, and 15% for storms with deep convective, wide convective, and broad stratiform echoes, respectively, when these rates are compared with a range of *Z-R* estimates [*Rasmussen et al.*, 2013].

4.3. Diurnal Variability

It is known that the diurnal cycle of cloudiness or rainfall in the hot spots peaks at night [*Killeen et al.*, 2007; *Halladay et al.*, 2012], whereas in the upper Andes and lower Amazon basin it peaks in the afternoon [*Garreaud and Wallace*, 1997; *Machado et al.*, 2002]. Recently, *Virts et al.* [2013] showed that lightning strokes are more frequent on the eastern Peruvian Andes during the night and early morning in NDJF. According to

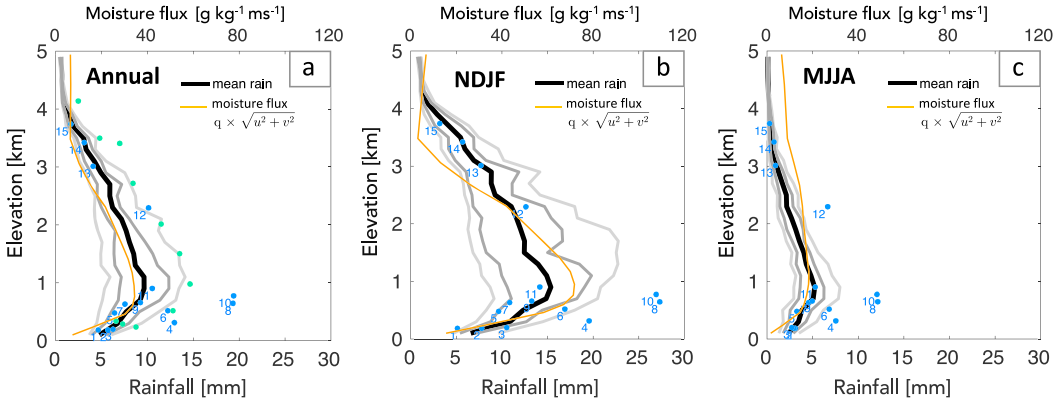

Figure 4. The rainfall variability between cross sections is shown as a function of terrain elevation (100 m bins) with the 10, 25, 75, and 90 percentiles (gray lines) and the mean (black) for the (a) annual, (b) NDJF, and (c) MJJA means. The blue dots correspond to the meteorological stations shown in Figures 1a and 3a), while the green dots in Figure 4c correspond to the Kosñipata transect (red in Figures 1a and 3a). The mean profile of the horizontal moisture flux (g kg^{-1} m s^{-1}) from ERA Interim is shown in orange in Figures 4c and 4d.

our analysis, the 22–09 LT period (Figure 5b) contains 70%–80% of the daily precipitation in NDJF on the eastern slope of the Andes and the inter-Andean valleys (up to 3500 m asl), as well as in a band parallel to the Andes in the Amazon (300–400 km from the 1000 m asl contour), and in the Titicaca lake [*Giovannettone and Barros*, 2009]. On the other hand, in almost all of the Andes above 3500 m asl, most of the rainfall ($>$ 80%) occurs between 10 and 21 LT (Figure 5a). Thus, we consider the periods of 22–09 and 10–21 LT as they capture most of the life cycle and associated rainfall of MCSs and capture the afternoon rainfall observed in the Andes over 3500 m asl.

Along the eastern Andes slopes, there is a diurnal minimum in precipitation in the afternoon (13–18 LT) (Figure 6a) associated with medium to small PFs (Figure 6c), with around 60% of the rainfall corresponding to the convective type (Figure 6a). Although the number of small PFs is much larger (Figure 6b), they contribute about as much as the medium PFs in terms of rainfall. In the hot spots, the depth of the convection is on the order of 4–5 km (Figure 6d). This is consistent with the development of the afternoon convection in the Amazon plains [*Machado et al.*, 2002; *Romatschke and Houze*, 2010].

Later in the evening, convective precipitation and lighning start developing on the eastern slopes, starting around 22–23 LT, primarily over terrain elevations of 1000–2000 m asl (Figures 6a and 7a and 7b), slightly higher than the mean SALLJ moisture transport peak (Figure 6a). This happens as the elevated afternoon heating of the Andes that drives upslope flow subsides [*Zängl and Egger*, 2005] and the SALJJ becomes

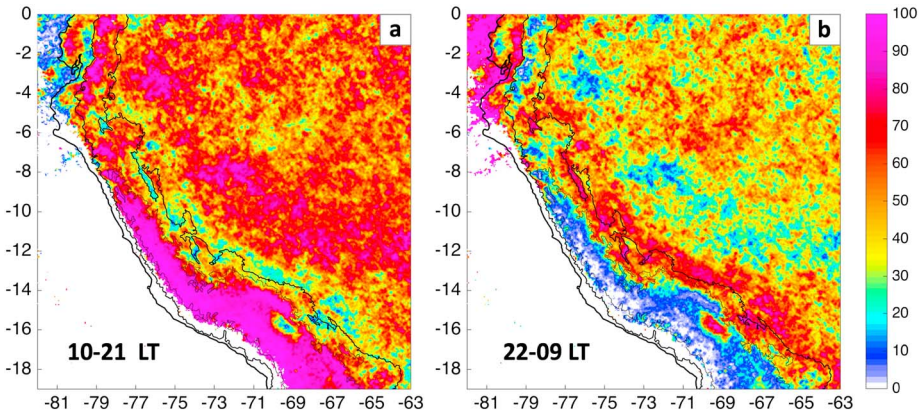

Figure 5. Percentage of the daily total NDJF TRMM 2A25 rainfall corresponding to (a) 10–21 LT and (b) 22–09 LT. The topographic contours of 1000 and 3500 m are shown as the black line and the thin black line, respectively.

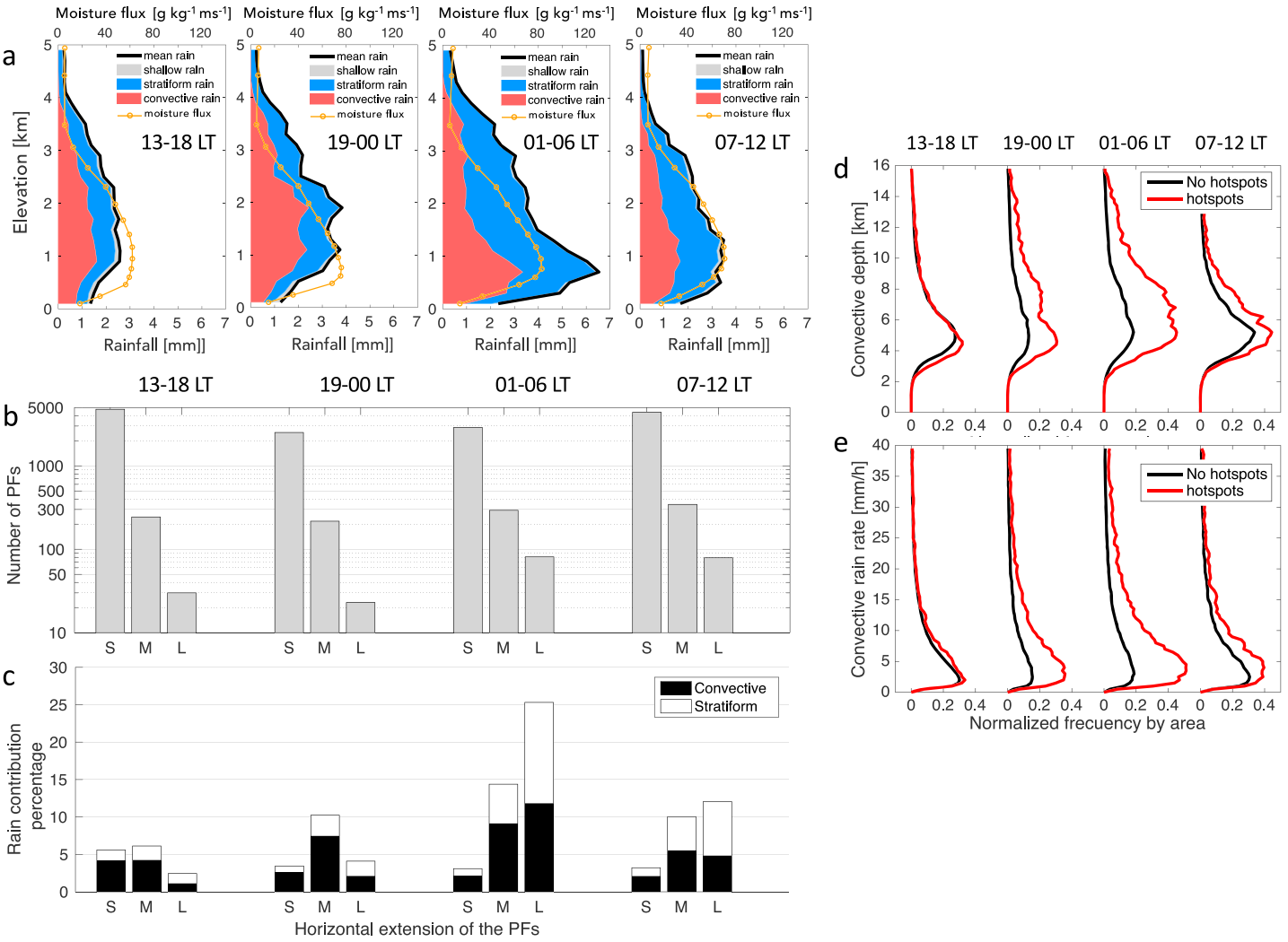

Figure 6. Mean diurnal cycle for NDJF from TRMM 2A25, using 6 h intervals, of (a) rainfall (mm) as a function of terrain elevation (black line, the area in red/blue/gray is the contribution of convective/stratiform/shallow rainfall) and the mean profile of the horizontal moisture flux (g kg^{-1} m s^{-1}) from ERA Interim is shown in orange; (b) the corresponding number of PFs observed on the slopes classified by size: small (S), medium (M), and large (L); (c) the contribution of the different sizes of PFs to the total daily rainfall in percentage (the contribution from convective and stratiform rainfall is shown in black and white respectively); and the distribution of (d) convective depth (echo-top minus topography) and of (e) convective rain rate in the hotspots and no hotspots (both distributions are normalized by the area of the corresponding regions).

therefore blocked by the Andes, forcing moisture convergence at those elevations [*Romatschke and Houze*, 2010]. The latter implies a larger mass flux by the SALLJ along the Andes at night (Figure 6a), consistent with the diurnal cycle of the SALLJ speed in the NCEP-NCAR Reanalysis further to the south [*Marengo et al.*, 2004]. However, the role of downslope flow in triggering convection [*Trachte et al.*, 2010a, 2010ab] cannot be ruled out. During this initial phase of the nocturnal convection, the number and rainfall contribution of the small PFs decreases, while the medium-sized PFs become the dominant contributors to rainfall, followed by large PFs (19–00 LT; Figure 6c). In the hot spots, the number of storms with depths between 6 and 14 km increases, peaking around 7–8 km (Figure 6d) and convective rain rate of $>$15 mm/h becomes more frequent (Figure 6e). All this indicates the increasing organization of the convective systems.

The lightning becomes more frequent after midnight (00–03 LT; Figure 7b), consistent with more intense convection indicated by heavier rainfall in the hot spots (00–03 LT; Figure 7a). At this time the number and rainfall contribution of large PFs increase greatly, dominating the latter, but with almost equal contributions from convective and stratiform precipitation (Figure 6c). This indicates that the storms have organized into MCSs, with their maximum convective precipitation displaced downslope [*Romatschke and Houze*, 2010] to

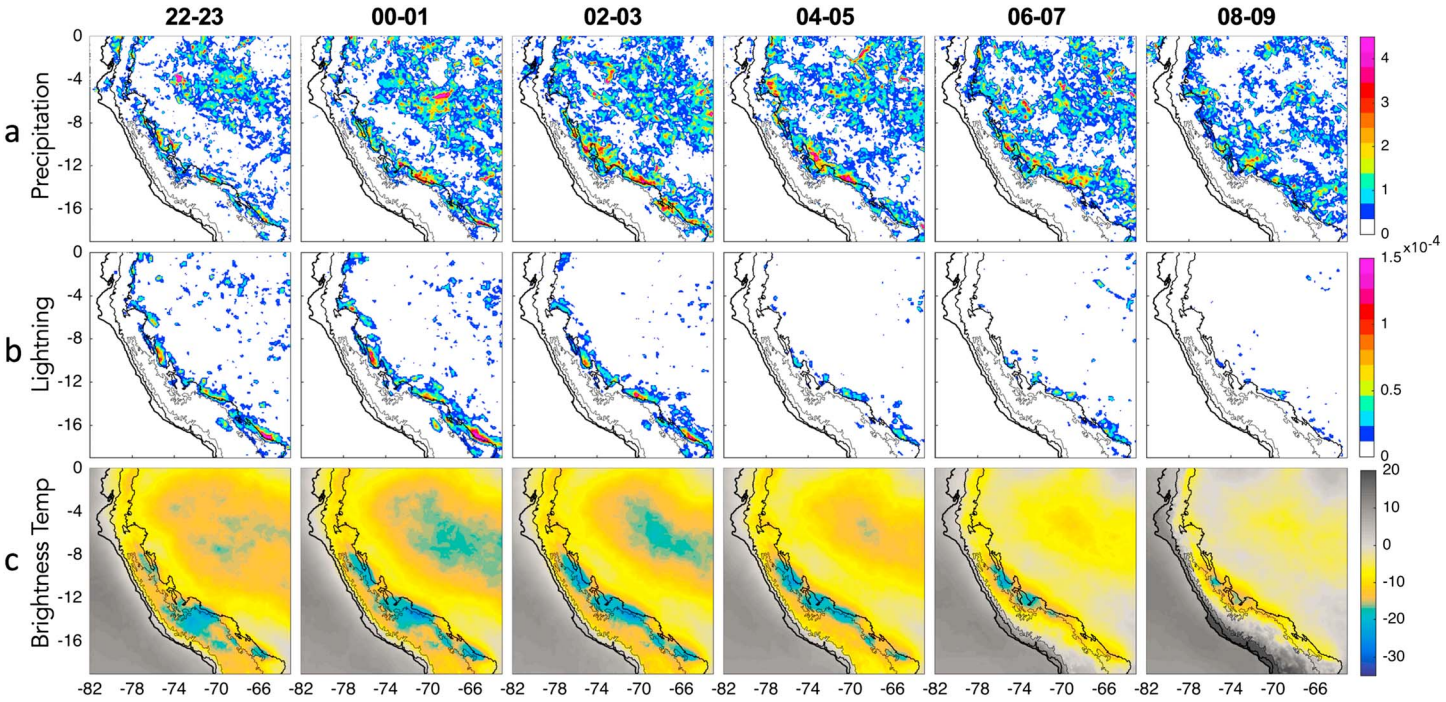

Figure 7. (a) TRMM 2A25 rainfall (mm), (b) WWLLN lightning frequency (strokes km^{-2} h^{-1}), and (c) GOES IR4 brightness temperature (°C) during NDJF for 2 h intervals between 22 and 09 LT. The topographic contours of 1000 and 3500 m are shown as the black line and the thin black line, respectively.

around 700 m asl, coincident with the peak in the mean SALLJ moisture transport at this time (Figure 6a), and a large stratiform component extending upslope, affecting higher locations [*Perry et al.*, 2013], and also downslope (01–06 LT; Figure 6a), as well as an increased number of storms with depths between 4 and 11 km (Figure 6d). The heavy precipitation continues through 04–05 LT (Figure 7a), but the intensity of the convection, according to the lightning activity, is reduced (Figure 7b). IR brightness temperatures indicate that the clouds extend over a wider region and persist until 07 LT (Figure 7c), which is typical of MCSs [*Houze*, 2004; *Salio et al.*, 2007; *Rozante and Cavalcanti*, 2008]. During the morning, the large PFs continue dominating the precipitation (07–12 LT; Figure 6c), but more subdued as the MCSs dissipate, while the precipitation rates become more spatially homogeneous between the hot spots and their surroundings (Figures 6e and 7a).

4.4. Synoptic Forcing

To investigate the influence of the synoptic-scale conditions on the occurrence of precipitation features (PFs) composites of daily ERA-Interim reanalysis wind and specific humidity anomalies at 850 hPa are shown (Figure 8) with the statistically significant wind anomalies as black vectors. The composite mean corresponding to when PFs of any size are observed (Figure 8a) shows a small but significant northerly wind anomaly in the western Amazon coming across the equator, consistent with previous studies [*Arraut and Satyamurty*, 2009; *Poveda et al.*, 2014]. Humidity, however, does not show signs of enhancement in this region and actually shows slightly negative large-scale anomalies. The mean vertical profile of horizontal moisture at two points (73.5°W, 9°S) and (69°W, 12°S) in the western Amazon when PFs of any size are observed is similar but stronger that the climatological one (Figure 9a). Likewise, the mean elevation-surface rainfall profile follows closely both vertical profiles of horizontal moisture flux (Figure 9a). The composite moisture flux profile for when only large PFs are present in the period of 1–13 LT, when more large PFs are observed and account for most of the precipitation (Figures 6b and 6c), is similar to the composite for PFs of any size (Figure 9b) but has large northerly wind anomalies (Figure 8b; note the different vector scale). Furthermore, this composite shows large southerly anomalies along the Andes to the south of 15°S converging into the eastern Andes of Peru. Also, positive specific humidity anomalies are found in the region around the hot spots. In order to better understand how this pattern arises, we subclassified the cases into southerly and northerly regimes based on the absolute 850 hPa meridional wind at the grid point (69°W, 12°S; green circle in Figure 8c). We found

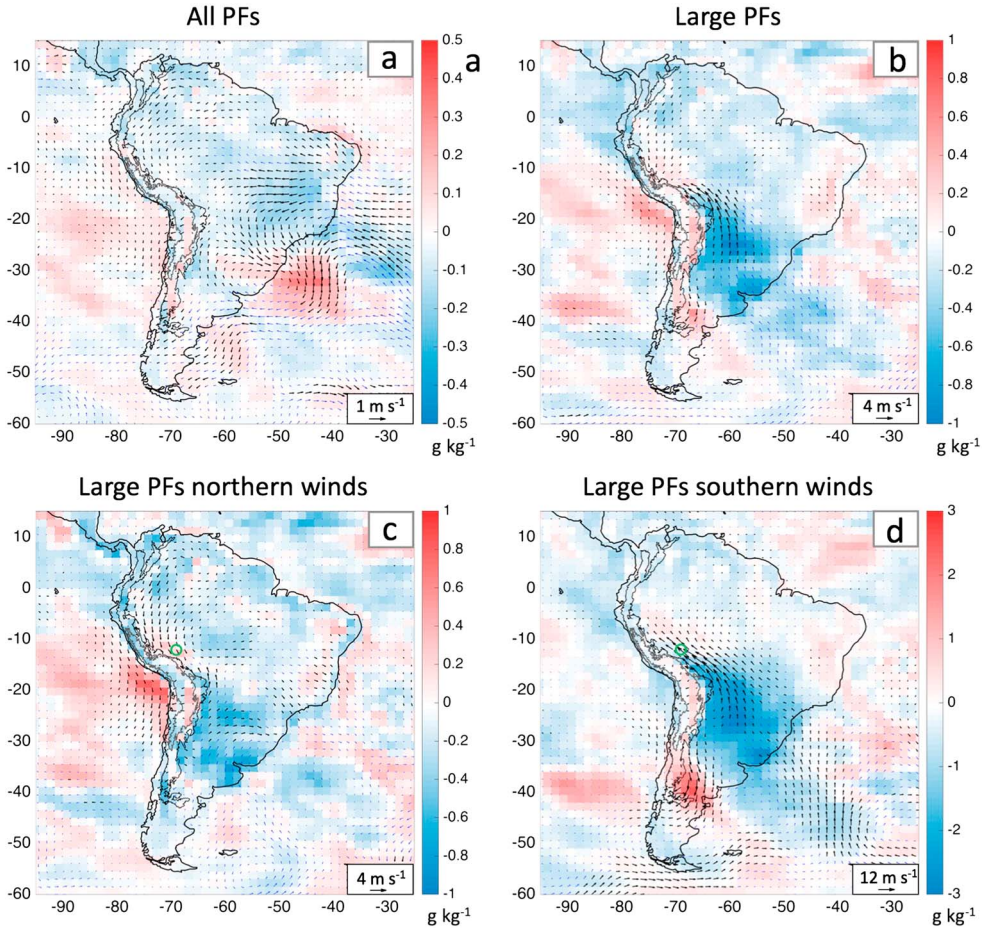

Figure 8. Mean wind (blue vectors) and specific humidity (color) anomalies in m s^{-1} and g kg^{-1}, respectively, from ERA Interim composites for (a) all-size PFs, (b) large size PFs between 1 and 13 LT, (c) large size PFs when northerly regime between 1 and 13 LT, and (d) large size PFs when southerly regime between 1 and 13 LT. The significant wind anomalies are the black vectors. The green circle is the reference grid point where wind direction in the composites is classified as southerly or northerly.

that 84% of the cases correspond to northerly winds and 16% to southerly winds. The election of the reference point affects slightly the number of composites of each regime, with fewer southerly cases as the point is displaced to the north. During the northerly wind/large-PF regime (Figure 8c), the northerly wind pattern is stronger in the western Amazon and positive specific humidity anomalies are observed between 7°S and 14°S, while southerly wind and negative specific humidity anomalies are found south of 18°S, indicating the weakening of the SALLJ in terms of moisture transport to southeastern South America. Likewise, the vertical profile of moisture flux for the northerly wind/large-PFs regime shows more than 50% enhancement in the SALLJ relative to the climatological profile (Figure 9b). The southerly wind/large-PF regime (Figure 8d) has strong mean wind anomalies that reach 14 m s^{-1} between 15° and 20°S and extend to 5°S. Additionally, negative specific humidity anomalies extend from southeastern South America to 15°S east of the Andes. The above are the signature of subtropical cold air incursions or surges along the eastern tropical Andes that in the warm season organize deep convection in the form of synoptic-scale bands of convective cloudiness along the frontal boundary that propagate equatorward [*Garreaud and Wallace*, 1998; *Garreaud*, 2000; *Garreaud*, 2001; Nieto *Ferreira et al.*, 2009]. Only half of the cold surges originating from the subtropics reach the equatorial regions [*Espinoza et al.*, 2013]. Due to their larger wind speed compared to the SALLJ, these surges transport slightly more moisture than the climatological winds at lower level (500–2500 m asl) (Figure 9b) but substantially higher moisture flux above 2500 m asl (Figure 9b), feeding precipitating systems in the eastern slopes of the Peruvian Andes but also at higher elevations. For example, in the

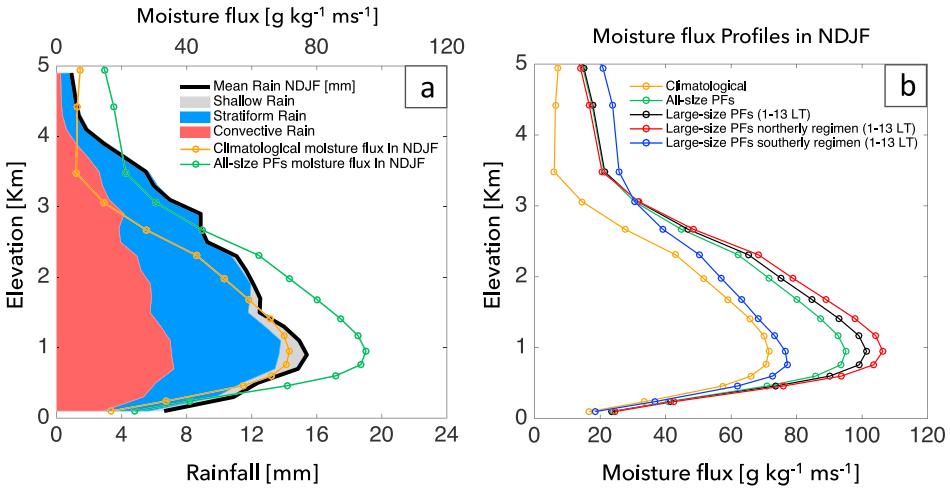

Figure 9. (a) Mean rainfall (mm) for NDJF from TRMM 2A25 in NDJF (black line) and the area in red/blue/gray is the contribution of convective/stratiform/shallow rainfall. The mean profiles of horizontal moisture flux (g kg^{-1} m s^{-1}) for climatological and all-size PF composites from ERA-Interim are shown in orange and green, respectively. (b) The mean profiles of horizontal moisture flux (g kg^{-1} m s^{-1}) from ERA Interim for climatological, all-size PFs, large-size PFs between 1 and 13 LT, large-size PFs when northerly regime between 1 and 13 LT, and large-size PFs when southerly regime between 1 and 13 LT are shown in orange, green, black, red, and blue, respectively.

Quelccaya ice cap (70.82°W, 13.93°S; 5670 m asl), most of the snow-height gain (~70%) is triggered by cold air incursions [*Hurley et al.*, 2015].

4.5. Triggering of Convection

The triggering mechanism of the observed MCSs during late night and early morning when cold surges passed through the region is well known [*Garreaud and Wallace*, 1998; *Garreaud*, 1999; *Garreaud*, 2001; *Espinoza et al.*, 2013]. However, the triggering mechanism when northerly winds is not obvious. We are inclined to agree with *Romatschke and Houze* [2010] that the convection in this region is triggered as the stronger SALLJ in the region is lifted over the foothills, but that this lifting is not effective during the daytime because heating of the mountains forces surface winds upslope and creates a strong divergence zone along the foothills that prevents convection there. Also, we cannot dismiss that nocturnal downslope winds converging with the moist flow from the Amazon basin along the Andes foothills could act as a triggering mechanism [*Giovannettone and Barros*, 2009; *Trachte et al.*, 2010a, 2010ab].

The available data and models appear inadequate to assess these mechanisms, and climate change might modify the different relevant factors in different directions. For instance, although specific humidity is expected to generally increase with warming [*Collins et al.*, 2013], models indicate that dynamical processes could weaken the SALLJ moisture flux and the precipitation on the eastern slopes [e.g., *Cook and Vizy*, 2008; *Marengo et al.*, 2012]. Even current high-resolution regional climate models have problems, greatly overestimating precipitation in the Andes (C. Junquas, personal communication), and it seems likely that the details of simulation of the convective processes will have to be improved in order for the projections to be more reliable. This in turn will require better observational data. The TRMM PR is an excellent unprecedented source of information, but it has strong biases and we are probably underestimating the relative contribution of deep convective regime. Focalized intensive in situ observations with aircrafts, wind profilers, ground-based radars, and/or atmospheric soundings would be valuable to provide a deeper understanding of this region and settle the triggering mechanism of convection.

5. Conclusions

We constructed a precipitation climatology at very high spatial resolution (0.05° × 0.05°) from the TRMM Precipitation Radar data (1998–2012). We used data from only one instrument to retain the native spatial resolution and to avoid known problems when merging with other instruments. Still, we show further evidence that the TRMM PR underestimates land precipitation, by up to 40% in the hot spots.

This study shows very strong yearlong rainfall in the precipitation hot spots that maximizes at a terrain elevation of 1000 m asl, extending slightly to the east. The precipitation in the hot spots is much larger than in the surroundings and is much larger in NDJF than in MJJA. The fine spatial structure of the climatology reveals that in the largest hot spot (13°S–14°S), in NDJF, there are two parallel bands of heavy rainfall, one on the top of a small 1000 m tall mountain chain and the other on the main Andean slope further downstream. Also, although the Andes generally block the moisture flux, rainfall is significant along the major inter-Andean valleys, the Pampas, Pachachaca, and Apurimac valley system (13°S–15°S, 74°W–72°W) that intrude from the Amazon into the Andes.

Based on rain gauge observations and the TRMM PR data, we established a clear relationship between surface precipitation and terrain elevation in the Andes-Amazon transition with a mean precipitation peak at an elevation of around 1000 m asl. That peak can be explained to first order by the vertical profile of the moisture transport by the SALLJ, which becomes blocked by the mountains at night as the upslope thermal forcing subsides, leading to mechanically forced convergence, feeding moisture to the convection that becomes organized into MCSs, which then moves downslope toward the Amazon.

Large precipitation features associated with mesoscale convective systems (MCS) are not frequent in the eastern slopes of the Andes; the most commonly observed PFs are small in terms of horizontal area. However, MCSs contribute at least 50% of the total precipitation on the eastern Andes, while small precipitation features contribute 15%. MCSs are observed, in 86% of the cases, when moisture transport converges along the slopes associated with a stronger SALLJ in this region but weaker in terms of its moisture transport to the south. The other 16% of the cases are associated with cold surges coming from the southeastern South America. In the afternoon (13–18 LT) MCSs are scarce and convection develops as is common in the Amazon plains.

Acknowledgments

This study was supported by the project "Study of the physical processes that control the superficial flows of energy and water for the model of frost, intense rains, and evapotranspiration in the central Andes of Peru" (PIBA-2-P-216-14). The GOES images were obtained from the NASA website at http://goes.gsfc.nasa.gov. The rain gauge data were obtained from the SENAMHI website at http://www.peruclima.pe/?p=data-historica. Thanks to NASA for the TRMM precipitation radar data, the data used in this effort were acquired as part of the activities of NASA's Science Mission Directorate and are archived and distributed by the Goddard Earth Sciences (GES) Data and Information Services Center (DISC). The data generated in this study are available at the IGP website at http://scah.igp.gob.pe/trmm. We are grateful to Jhan Carlo Espinoza for his help with the SENAMHI data and Yamina Silva the principal investigator of the project PIBA-2-P-216-14.

References

Arraut, J. M., and P. Satyamurty (2009), Precipitation and water vapor transport in the Southern Hemisphere with emphasis on the South American region, *J. Appl. Meteorol. Climatol.*, *48*(9), 1902–1912.

Barnes, J., T. Ehlers, N. Insel, N. McQuarrie, and C. Poulsen (2012), Linking orography, climate, and exhumation across the central Andes, *Geology*, doi:10.1130/G33229.1.

Basist, A., G. D. Bell, and V. Meentemeyer (1994), Statistical relationships between topography and precipitation patterns, *J. Clim.*, *7*(9), 1305–1315.

Bendix, J., K. Trachte, J. Cermak, R. Rollenbeck, and T. Nauß (2009), Formation of convective clouds at the foothills of the tropical eastern Andes (South Ecuador), *J. Appl. Meteorol. Climatol.*, *48*(8), 1682–1695.

Berbery, E. H., and V. R. Barros (2002), The hydrologic cycle of the La Plata basin in South America, *J. Hydrometeorol.*, *3*(6), 630–645.

Biasutti, M., S. E. Yuter, C. D. Burleyson, and A. H. Sobel (2012), Very high resolution rainfall patterns measured by TRMM precipitation radar: seasonal and diurnal cycles, *Clim. Dyn.*, *39*(1–2), 239–258.

Berrisford, P., D. Dee, P. Poli, R. Brugge, K. Fielding, M. Fuentes, P. Kallberg, S. Kobayashi, S. Uppala, and A. Simmons (2011), The ERA-Interim archive version 2.0, *ERA Rep. Ser. 1*, ECMWF, Shinfield Park, Reading, U. K., 13177.

Bookhagen, B., and M. Strecker (2008), Orographic barriers, high-resolution TRMM rainfall, and relief variations along the eastern Andes, *Geophys. Res. Lett.*, *35*, L06403, doi:10.1029/2007GL032011.

Collins, M., et al. (2013), Long-term climate change: Projections, commitments and irreversibility, in *Climate Change 2013: The Physical Science Basis. Contribution of Working Group I to the Fifth Assessment Report of the Intergovernmental Panel on Climate Change*, edited by T. F. Stocker et al., 1032 pp., Cambridge Univ. Press, Cambridge, U. K., and New York.

Cook, K. H., and E. K. Vizy (2008), Effects of twenty-first-century climate change on the Amazon rain forest, *J. Clim.*, *21*(3), 542-560.

Dee, D., et al. (2011), The ERA-Interim reanalysis: Configuration and performance of the data assimilation system, *Q. J. R. Meteorol. Soc.*, *137*(656), 553–597, doi:10.1002/qj.828.

Douglas, M. W., M. Nicolini, and C. Saulo (1999), The low-level jet at Santa Cruz, Bolivia during January–March 1998: Pilot balloon observation and model comparisons. Preprints, *10th Symp. on Global Change, Am*. Meteorol. Soc., pp. 223–226, Dallas, Tex.

Espinoza, J. C., J. Ronchail, M. Lengaigne, N. Quispe, Y. Silva, M. L. Bettolli, G. Avalos, and A. Llacza (2013), Revisiting wintertime cold air intrusions at the east of the Andes: Propagating features from subtropical Argentina to Peruvian Amazon and relationship with large-scale circulation patterns, *Clim. Dyn.*, *41*(7–8), 1983–2002.

Espinoza, J. C., S. Chavez, J. Ronchail, C. Junquas, K. Takahashi, and W. Lavado (2015), Rainfall hotspots over the southern tropical Andes: Spatial distribution, rainfall intensity, and relations with large-scale atmospheric circulation, *Water Resour. Res.*, *51*, 3459–3475, doi:10.1002/2014WR016273.

Espinoza Villar, J. C., J. Ronchail, J. L. Guyot, G. Cochonneau, F. Naziano, W. Lavado, E. De Oliveira, R. Pombosa, and P. Vauchel (2009), Spatio-temporal rainfall variability in the Amazon basin countries (Brazil, Peru, Bolivia, Colombia, and Ecuador), *Int. J. Climatol.*, *29*(11), 1574–1594, doi:10.1002/joc.1791.

Ferreira, R. N., T. M. Rickenbach, D. L. Herdies, and L. M. Carvalho (2003), Variability of South American convective cloud systems and tropospheric circulation during January–March 1998 and 1999, *Mon. Weather Rev.*, *131*(5), 961–973.

Figueroa, S. N., and C. A. Nobre (1990), Precipitation distribution over central and western tropical South America, *Climanalise*, *5*(6), 36–45.

Garreaud, R. (1999), Cold air incursions over subtropical and tropical South America: A numerical case study, *Mon. Weather Rev.*, *127*(12), 2823–2853.

Garreaud, R. (2000), Cold air incursions over subtropical South America: Mean structure and dynamics, *Mon. Weather Rev.*, *128*(7), 2544–2559.

Garreaud, R., and J. M. Wallace (1998), Summertime incursions of midlatitude air into subtropical and tropical South America, *Mon. Weather Rev.*, *126*(10), 2713–2733.
Garreaud, R., and J. M. Wallace (1997), The diurnal march of convective cloudiness over the Americas, *Mon. Weather Rev.*, *125*(12), 3157–3171.
Garreaud, R. D. (2001), Subtropical cold surges: Regional aspects and global distribution, *Int. J. Climatol.*, *21*(10), 1181–1197.
Giovannettone, J., and A. Barros (2009), Probing regional orographic controls of precipitation and cloudiness in the central Andes using satellite data, *J. Hydrometeorol.*, *10*(1), 167–182.
Hamada, A., and Y. N. Takayabu (2014), A removal filter for suspicious extreme rainfall profiles in TRMM PR 2A25 version-7 data, *J. Appl. Meteorol. Climatol.*, *53*(5), 1252–1271.
Halladay, K., Y. Malhi, and M. New (2012), Cloud frequency climatology at the Andes/Amazon transition: 1. Seasonal and diurnal cycles, *J. Geophys. Res.*, *117*, D23102, doi:10.1029/2012JD017770.
Hirose, M., R. Oki, S. Shimizu, M. Kachi, and T. Higashiuwatoko (2008), Finescale diurnal rainfall statistics refined from eight years of TRMM PR data, *J. Appl. Meteorol. Climatol.*, *47*, 544–561, doi:10.1175/2007JAMC1559.1.
Hoorn, C., et al. (2010), Amazonia through time: Andean uplift, climate change, landscape evolution, and biodiversity, *Science*, *330*(6006), 927–931.
Horton, B. K. (1999), Erosional control on the geometry and kinematics of thrust belt development in the central Andes, *Tectonics*, *18*, 1292–1304, doi:10.1029/1999TC900051.
Houze, R. A. (2004), Mesoscale convective systems, *Rev. Geophys.*, *42*, RG4003, doi:10.1029/2004RG000150.
Houze, R. A. (2012), Orographic effects on precipitating clouds, *Rev. Geophys.*, *50*, RG1001, doi:10.1029/2011RG000365.
Houze, R. A., D. C. Wilton, and B. F. Smull (2007), Monsoon convection in the Himalayan region as seen by the TRMM Precipitation Radar, *Q. J. R. Meteorol. Soc.*, *133*(627), 1389–1411.
Hurley, J. V., M. Vuille, D. R. Hardy, S. J. Burns, and L. G. Thompson (2015), Cold air incursions, δ18O variability, and monsoon dynamics associated with snow days at Quelccaya Ice Cap, Peru, *J. Geophys. Res. Atmos.*, *120*, 7467–7487, doi:10.1002/2015JD023323.
Iguchi, T., T. Kozu, R. Meneghini, J. Awaka, and K. I. Okamoto (2000), Rain-profiling algorithm for the TRMM precipitation radar, *J. Appl. Meteorol.*, *39*(12), 2038–2052.
Iguchi, T., T. Kozu, J. Kwiatkowski, R. Meneghini, J. Awaka, and K. Okamoto (2009), Uncertainties in the rain profiling Algorithm for the TRMM precipitation radar, *J. Meteorol. Soc. Jpn.*, *87A*, 1–30, doi:10.2151/jmsj.87A.1.
Killeen, T. J., M. Douglas, T. Consiglio, P. M. Jørgensen, and J. Mejia (2007), Dry spots and wet spots in the Andean hotspot, *J. Biogeogr.*, *34*(8), 1357–1373, doi:10.1111/j.1365-2699.2006.01682.x.
Kishore, P., M. V. Ratnam, S. P. Namboothiri, I. Velicogna, G. Basha, J. H. Jiang, K. Igarashi, S. V. B. Rao, and V. Sivakumar (2011), Global (50° S–50° N) distribution of water vapor observed by COSMIC GPS RO: Comparison with GPS radiosonde, NCEP, ERA-Interim, and JRA-25 reanalysis data sets, *J. Atmos. Sol. Terr. Phys.*, *73*(13), 1849–1860.
Kirstetter, P. E., Y. Hong, J. J. Gourley, M. Schwaller, W. Petersen, and J. Zhang (2013), Comparison of TRMM 2a25 products, version 6 and version 7, with NOAA/NSSL ground radar-based National Mosaic QPE, *J. Hydrometeorol.*, *14*(2), 661–669.
Kozu, T., T. Iguchi, T. Shimomai, and N. Kashiwagi (2009), Raindrop size distribution modeling from a statistical rain parameter relation and its application to the TRMM precipitation radar rain retrieval algorithm, *J. Appl. Meteorol. Climatol.*, *48*(4), 716–724, doi:10.1175/2008JAMC1998.1.
Kummerow, C., Y. Hong, W. S. Olson, S. Yang, R. F. Adler, J. McCollum, R. Ferraro, G. Petty, D.-B. Shin, and T. T. Wilheit (2001), The evolution of the Goddard Profiling Algorithm (GPROF) for rainfall estimation from passive microwave sensors, *J. Appl. Meteorol.*, *40*(11), 1801–1820.
Liu, C. (2011), Rainfall contributions from precipitation systems with different sizes, convective intensities, and durations over the tropics and subtropics, *J. Hydrometeorol.*, *12*(3), 394–412.
Liu, C., E. J. Zipser, D. J. Cecil, S. W. Nesbitt, and S. Sherwood (2008), A cloud and precipitation feature database from nine years of TRMM observations, *J. Appl. Meteorol. Climatol.*, *47*(10), 2712–2728, doi:10.1175/2008JAMC1890.1.
Lowman, L. E., and A. P. Barros (2014), Investigating links between climate and orography in the central Andes: Coupling erosion and precipitation using a physical-statistical model, *J. Geophys. Res. Earth Surf.*, *119*, 1322–1353, doi:10.1002/2013JF002940.
Machado, L. A., H. Laurent, and A. A. Lima (2002), Diurnal march of the convection observed during TRMM-WETAMC/LBA, *J. Geophys. Res.*, *107*(D20), 8064, doi:10.1029/2001JD000338.
Magrin, G. O., J. A. Marengo, J.-P. Boulanger, M. S. Buckeridge, E. Castellanos, G. Poveda, F. R. Scarano, and S. Vicuña (2014), Central and South America, in *Climate Change 2014: Impacts, Adaptation, and Vulnerability. Part B: Regional Aspects. Contribution of Working Group II to the Fifth Assessment Report of the Intergovernmental Panel on Climate Change*, pp. 1499–1566, Cambridge Univ. Press, Cambridge, U. K., and New York.
Marengo, J. A., W. R. Soares, C. Saulo, and M. Nicolini (2004), Climatology of the low-level jet east of the Andes as derived from the NCEP-NCAR reanalyses: Characteristics and temporal variability, *J. Clim.*, *17*(12), 2261–2280.
Marengo, J. A., et al. (2012), Development of regional future climate change scenarios in South America using the Eta CPTEC/HadCM3 climate change projections: Climatology and regional analyses for the Amazon, São Francisco and the Paraná River basins, *Clim. Dyn.*, doi:10.1007/s00382-011-1155-5.
McQuarrie, N., T. Ehlers, J. Barnes, and B. Meade (2008), Temporal variation in climate and tectonic coupling in the central Andes, *Geology*, doi:10.1130/G25124A.1.
Mohr, K. I., D. Slayback, and K. Yager (2014), Characteristics of precipitation features and annual rainfall during the TRMM era in the central Andes, *J. Clim.*, *27*(11), 3982–4001.
Myers, N., R. A. Mittermeier, C. G. Mittermeier, G. A. Da Fonseca, and J. Kent (2000), Biodiversity hotspots for conservation priorities, *Nature*, *403*(6772), 853–858.
Negri, A. J., E. N. Anagnostou, and R. F. Adler (2000), A 10-yr climatology of Amazonian rainfall derived from passive microwave satellite observations, *J. Appl. Meteorol.*, *39*(1), 42–56.
Nesbitt, S. W., and A. M. Anders (2009), Very high resolution precipitation climatologies from the Tropical Rainfall Measuring Mission precipitation radar, *Geophys. Res. Lett.*, *36*, L15815, doi:10.1029/2009GL038026.
Nogués-Paegle, J., and K. C. Mo (1997), Alternating wet and dry conditions over South America during summer, *Mon. Weather Rev.*, *125*(2), 279–291.
Pauluis, O., and J. Dias (2012), Satellite estimates of precipitation-induced dissipation in the atmosphere, *Science*, *335*(6071), 953–956, doi:10.1126/science.1215869.
Pepin, E., J. L. Guyot, E. Armijos, H. Bazan, P. Fraizy, J. S. Moquet, L. Noriega, W. Lavado, R. Pombosa, and P. Vauchel (2013), Climatic control on eastern Andean denudation rates (Central Cordillera from Ecuador to Bolivia), *J. South Amer. Earth Sci.*, *44*, 85–93.
Perry, L. B., A. Seimon, and G. M. Kelly (2013), Precipitation delivery in the tropical high Andes of southern Peru: New findings and paleoclimatic implications, *Int. J. Climatol.*, doi:10.1002/joc.3679.

Poveda, G., L. Jaramillo, and L. F. Vallejo (2014), Seasonal precipitation patterns along pathways of South American low-level jets and aerial rivers, *Water Resour. Res.*, *50*, 98–118, doi:10.1002/2013WR014087.
Rapp, J., and M. Silman (2012), Diurnal, seasonal, and altitudinal trends in microclimate across a tropical montane cloud forest, *Clim. Res.*, *55*, 17–32, doi:10.3354/cr01127.
Rasmussen, K. L., S. L. Choi, M. D. Zuluaga, and R. A. Houze (2013), TRMM precipitation bias in extreme storms in South America, *Geophys. Res. Lett.*, *40*, 3457–3461, doi:10.1002/grl.50651.
Rasmussen, K. L., M. M. Chaplin, M. D. Zuluaga, and R. A. Houze Jr. (2016), Contribution of extreme convective storms to rainfall in South America, *J. Hydrometeorol.*, *17*(1), 353–367, doi:10.1175/JHM-D-15-0067.1.
Roe, G. H., K. X. Whipple, and J. K. Fletcher (2008), Feedbacks among climate, erosion, and tectonics in a critical wedge orogen, *Am. J. Sci.*, doi:10.2475/07.2008.01.
Romatschke, U., and R. A. Houze Jr. (2010), Extreme summer convection in South America, *J. Clim.*, *23*(14), 3761–3791, doi:10.1175/2010JCLI3465.1.
Romatschke, U., and R. A. Houze Jr. (2013), Characteristics of precipitating convective systems accounting for the summer rainfall of tropical and subtropical South America, *J. Hydrometeorol.*, *14*(1), 25–46, doi:10.1175/JHM-D-12-060.1.
Rozante, J. R., and I. F. A. Cavalcanti (2008), Regional Eta model experiments: SALLJEX and MCS development, *J. Geophys. Res.*, *113*, D17106, doi:10.1029/2007JD009566.
Sacek, V. (2014), Drainage reversal of the Amazon River due to the coupling of surface and lithospheric processes, *Earth Planet. Sci. Lett.*, doi:10.1016/j.epsl.2014.06.022.
Salio, P., M. Nicolini, and E. J. Zipser (2007), Mesoscale convective systems over southeastern South America and their relationship with the South American low-level jet, *Mon. Weather Rev.*, *135*(4), 1290–1309, doi:10.1175/MWR3305.1.
Saulo, A. C., M. Nicolini, and S. C. Chou (2000), Model characterization of the South American low-level flow during the 1997–1998 spring–summer season, *Clim. Dyn.*, *16*(10), 867–881.
Seto, S., and T. Iguchi (2007), Rainfall-induced changes in actual surface backscattering cross sections and effects on rain-rate estimates by spaceborne precipitation radar, *J. Atmos. Ocean. Technol.*, *24*(10), 1693–1709.
Trachte, K., and J. Bendix (2012), Katabatic flows and their relation to the formation of convective clouds—Idealized case studies, *J. Appl. Meteorol. Climatol.*, *51*(8), 1531–1546, doi:10.1175/JAMC-D-11-0184.1.
Trachte, K., R. Rollenbeck, and J. Bendix (2010a), Nocturnal convective cloud formation under clear-sky conditions at the eastern Andes of south Ecuador, *J. Geophys. Res.*, *115*, D24203, doi:10.1029/2010JD014146.
Trachte, K., T. Nauss, and J. Bendix (2010b), The impact of different terrain configurations on the formation and dynamics of katabatic flows: Idealised case studies, *Boundary Layer Meteorol.*, *134*, 307–325, doi:10.1007/s10546-009-9445-8.
Vera, C., et al. (2006a), The South American low-level jet experiment, *Bull. Am. Meteorol. Soc.*, *87*(1), 63–77, doi:10.1175/BAMS-87-1-63.
Vera, C., et al. (2006b), Toward a unified view of the American monsoon systems, *J. Clim.*, *19*(20), 4977–5000, doi:10.1175/JCLI3896.1.
Virts, K. S., J. M. Wallace, M. L. Hutchins, and R. H. Holzworth (2013), Highlights of a new ground-based, hourly global lightning climatology, *Bull. Am. Meteorol. Soc.*, *94*(9), 1381–1391.
Weinreb, M., and Han, D. (2011), Conversion of GVAR infrared data to scene radiance or temperature. [Available at http://www.ospo.noaa.gov/Operations/GOES/calibration/gvar-conversion.html.]
Zängl, G., and J. Egger (2005), The diurnal circulation of the Bolivian Altiplano. Part II: Theoretical aspects, Mon. Weather Rev.